Dalton Transactions

ROYAL SOCIETY OF CHEMISTRY

PAPER

View Article Online
View Journal | View Issue

Check for updates

Cite this: *Dalton Trans.*, 2026, **55**, 5189

Double second-order Jahn–Teller strategy driven NLO response in sulfate crystal $Nb_2O_2(TeO_3)_2(SO_4)$ with a large birefringence

Jingsha Xu,[a] Xiaofeng Zhang,[b] Shanshan Chen,[c] Weiyi Wang,[c] Wenbo Qiu,[c] Weizhao Cai *[c] and Liujiang Zhou *[a,d]

Nonlinear optical (NLO) crystals serve as indispensable components in laser technology. Many modifications of sulfate-based NLO materials rely on introducing a single type of functional cation, which in some cases leads to an imbalanced improvement in either NLO response or birefringence. To enable simultaneous improvement of these key properties, we designed and synthesized a novel sulfate compound, $Nb_2O_2(TeO_3)_2(SO_4)$, using a double second-order Jahn–Teller (SOJT) strategy that introduces both Nb^{5+} (d^0 cation) and Te^{4+} (lone-pair cation) into the sulfate framework. Remarkably, the introduction of distorted [NbO_6] octahedra and [TeO_3] pyramids enables the material to achieve a remarkable birefringence of 0.197 at 546 nm and a second-harmonic generation (SHG) response 0.82 times that of KH_2PO_4 (KDP). Furthermore, the compound exhibits high thermal stability (>600 °C), maintains chemical stability in both water and concentrated sulfuric acid, and possesses an ultraviolet (UV) cutoff edge at 305 nm. Theoretical analyses confirm that the synergy between the [NbO_6] octahedra and the [TeO_3] pyramids is the key mechanism for the enhanced SHG response and birefringence. This work demonstrates the potential of $Nb_2O_2(TeO_3)_2(SO_4)$ as a UV-NLO material and validates the effectiveness of the multi-component synergistic strategy in designing advanced NLO crystals.

Received 25th December 2025,
Accepted 5th March 2026

DOI: 10.1039/d5dt03078a

rsc.li/dalton

Published on 06 March 2026. Downloaded on 6/21/2026 11:58:36 AM.

Introduction

In modern laser science and technology, ultraviolet (UV) nonlinear optical (NLO) materials serve as critical components for laser wavelength conversion and are widely used in precision micromachining, photolithography, and biomedical imaging.[1–5] This is because they can effectively extend the wavelength range of commonly used laser sources through frequency conversion processes such as second-harmonic generation (SHG).[6] As is well known, high-performance NLO materials are typically required to possess a non-centrosymmetric (NCS) structure, a relatively large SHG coefficient, a wide UV transparency window, appropriate birefringence, good stability, and crystal growth ability.[7–10] However, these performance parameters are often subject to restrictive relationships, which pose severe challenges to the design and preparation of high-performance UV-NLO materials.[11–14] Therefore, the exploration of novel UV-NLO candidate compounds is required.

Traditionally, the design strategies of NLO materials have primarily focused on incorporating π-conjugated planar anionic groups, such as [CO_3], [BO_3], [NO_3], [B_3O_6], and [$C_3N_3O_3$], due to their capacity for strong SHG response and birefringence.[15–22] However, such materials generally suffer from narrow UV transparency windows and poor thermal stability. In recent years, researchers have shifted their attention to non-π-conjugated [SO_4] tetrahedral groups, which can endow materials with a wider UV transparency window and higher thermal stability,[23,24] such as $Li_9Na_3Rb_2(SO_4)_7$[25] and $NH_4NaLi_2(SO_4)_2$.[26] However, due to the small microscopic second-order polarizability and weak structural anisotropy of tetrahedral groups, most of these crystals exhibit weak SHG signals and/or small birefringence. For instance, the birefringence of $LiNH_4SO_4$ is only 0.0078 at 532 nm,[27] which severely limits its practical applications.

To overcome the inherent limitations of sulfates, the introduction of cations susceptible to second-order Jahn–Teller (SOJT) distortions has proven to be an effective strategy, such as stereochemically active lone pairs of electrons (SCALP) (*e.g.*, Bi^{3+}, Te^{4+}, and Sb^{3+})[11,28,29] and octahedrally coordinated d^0 cations (*e.g.*, Nb^{5+}, Ti^{4+}, and Mo^{6+}).[30–36] SCALP cations such as

[a]*School of Physics, State Key Laboratory of Electronic Thin Films and Integrated Devices, University of Electronic Science and Technology of China, Chengdu 611731, China. E-mail: ljzhou@uestc.edu.cn*
[b]*School of Electronic and Electrical Engineering, Chongqing University of Science and Technology, Chongqing 401331, China*
[c]*School of Materials and Energy, University of Electronic Science and Technology of China, Chengdu 611731, China. E-mail: wzhcai@uestc.edu.cn*
[d]*Institute of Fundamental and Frontier Sciences, University of Electronic Science and Technology of China, Chengdu 611731, China*

Published on 06 March 2026. Downloaded on 6/21/2026 11:58:36 AM.

Te^{4+} typically form asymmetric coordination polyhedra (*e.g.*, [TeO_3] pyramids or [TeO_4] polyhedra), whose intrinsic structural anisotropy, amplified by the directional arrangement of lone pairs, is highly effective for generating large birefringence, as observed in various sulfate–tellurite systems.[37–40] Meanwhile, d^0 cations like Nb^{5+} ions tend to form distorted [NbO_6] octahedra, and such structural units can generate significant local polarization, effectively promoting the formation of NCS structures and enhancing macroscopic nonlinear optical responses.[34,41–45] Many current modifications still rely on introducing only one type of SOJT-active cation, which in some cases results in selective enhancement of either birefringence or NLO response, such as $In_3(SO_4)(TeO_3)_2F_3(H_2O)$ (0.11 × KDP, 0.0876@1064 nm)[38] and $K_4Sb(SO_4)_3Cl$ (0.1 × KDP, 0.068@546 nm).[13] Theoretically, the co-incorporation of these two distinct types of SOJT-active units within a common sulfate matrix could enable coupling between the geometric anisotropy driven by SCALP cations and the electronic polarization induced by d^0 cations, potentially leading to improvement of both key optical properties.[45,46] However, research on sulfate systems capable of integrating both SCALP cations and d^0 cations remains limited. Therefore, there is significant potential to grow high-performance NLO crystals using a dual-SOJT cooperative strategy.

Motivated by this concept, we herein introduce [NbO_6] octahedra and [TeO_3] pyramids into a single sulfate framework to synthesize a novel sulfate compound, $Nb_2O_2(TeO_3)_2(SO_4)$, by the hydrothermal method. Property measurements reveal that this material retains the wide UV transparency and high thermal stability (>600 °C) of sulfates, while exhibiting a moderate SHG response of approximately 0.82 times that of KH_2PO_4 (KDP) and a remarkable birefringence of 0.197 at 546 nm, indicating its great potential as a UV-NLO material.

Experimental details

Reagents

Nb_2O_5 (≥99.99%, Aladdin), TeO_2 (99.99%, Aladdin), and H_2SO_4 (98%, Chengdu Jinshan Chemical Reagent) are analytical grade and were used without further purification.

Synthesis

Single crystals of $Nb_2O_2(TeO_3)_2(SO_4)$ were successfully obtained via a hydrothermal reaction. A mixture of Nb_2O_5 (0.0399 g, 0.15 mmol), TeO_2 (0.1197 g, 0.75 mmol), H_2SO_4 (2 mL), and deionized water (1 mL) was stirred magnetically for 15–20 minutes and then transferred into a 25 mL Teflon-lined stainless-steel autoclave. The sealed autoclave was heated at 230 °C for 3 days and then cooled to 30 °C at a rate of 2 °C h^{-1}. The possible chemical reaction for this reaction should be $Nb_2O_5 + TeO_2 + H_2SO_4 \rightarrow Nb_2O_2(TeO_3)_2(SO_4) + H_2O$. The reaction product was washed with deionized water and dried in air at 50 °C for 3 hours. Pure colorless and transparent plate-like $Nb_2O_2(TeO_3)_2(SO_4)$ crystals were isolated under a microscope, with a yield of about 51% (based on Nb element).

Single-crystal X-ray diffraction

The single-crystal X-ray diffraction (SCXRD) data of $Nb_2O_2(TeO_3)_2(SO_4)$ were collected using a Bruker D8 Quest diffractometer with a Phonon III detector and four-cycle kappa geometry, and an Incoatec IμS 3.0 Mo-Kα microfocus source (λ = 0.71073 Å). The measurements were carried out at 296.00 K. The APEX5 software package was used to conduct data collection and reduction.[47] The structure was solved through direct methods using SHELXS-1997 and refined with the XL refinement package using least-squares minimization, with the chemical formula of the compound determined.[48] Based on the diffraction data, two possible space groups, *Cc* and *C*2/*c*, were considered. Although the refinement results for both space groups were equally good, *Cc* was selected due to the observed SHG response, which dictates that the space group must be non-centrosymmetric. The structural model was examined for missed symmetry using the PLATON program, and no additional crystallographic symmetry consistent with the diffraction data was detected.[49] The relevant crystal data and structure refinement details of $Nb_2O_2(TeO_3)_2(SO_4)$ are given in Table S1. Atomic coordinates, equivalent isotropic displacement parameters, bond valence sums, selected bond lengths, and bond angles are listed in Tables S2–S4.

Powder X-ray diffraction

Powder X-ray diffraction (PXRD) data for $Nb_2O_2(TeO_3)_2(SO_4)$ were collected using a Bruker D2 PHASER diffractometer equipped with graphite-monochromated Cu-Kα radiation (λ = 1.5406 Å). The measurement was performed over a 2θ range from 5° to 70° with a step size of 0.02° and a scan rate of 0.1 s per step.

Thermal analysis

Thermogravimetric analysis (TGA) and differential scanning calorimetry (DSC) measurements of the $Nb_2O_2(TeO_3)_2(SO_4)$ sample were performed using a NETZSCH STA 449F5 simultaneous thermal analyzer under a nitrogen atmosphere. Approximately 7.14 mg of the sample was loaded into an Al_2O_3 crucible and heated from room temperature to 1200 °C at a heating rate of 10 °C·min^{-1}.

Infrared spectroscopy

Fourier transform infrared (FTIR) spectroscopy of $Nb_2O_2(TeO_3)_2(SO_4)$ was performed using a Bruker INVENIO R Fourier transform infrared spectrometer at room temperature, over the wavenumber range of 4000–400 cm^{-1}.

UV-Vis-NIR diffuse reflectance spectra

The UV-Vis-NIR diffuse reflectance spectra of $Nb_2O_2(TeO_3)_2(SO_4)$ were recorded at room temperature using a LAMBDA 1050+ UV/Vis/NIR spectrophotometer, covering a wavelength range of 200–2500 nm. The reflectance spectra were converted into absorption spectra using the Kubelka–Munk function $K/S = F(R) = (1 - R)^2/2R$, where S is the scattering coefficient, K is the absorption coefficient, and R is the reflectance.[50]

This journal is © The Royal Society of Chemistry 2026

Published on 06 March 2026. Downloaded on 6/21/2026 11:58:36 AM.

Second-harmonic generation measurements

The SHG response of a $Nb_2O_2(TeO_3)_2(SO_4)$ single crystal was measured using a home-designed goLite solution-NLO system. A 1064 nm pulsed fiber laser was used as the excitation source, and experiments were conducted by varying its output power. The SHG signals were collected using a spectrometer (NVOA2S-EX). The system was validated with a KDP single crystal before starting the measurements. The Bruker D8 Quest diffractometer was used to determine the crystal plane orientation of the crystal under test. Additionally, the SHG efficiency of polycrystalline crystals with different particle sizes was measured under irradiation from a Q-switched Nd:YAG laser at 1064 nm, using the Kurtz–Perry method.[51] Since the SHG intensity is dependent on particle size, $Nb_2O_2(TeO_3)_2(SO_4)$ crystals were ground and sieved into several particle size ranges (30–46, 46–60, 60–75, 75–125, 125–150, and 150–214 μm), and KDP microcrystals with corresponding size ranges served as references.

Birefringence measurement

The birefringence of an $Nb_2O_2(TeO_3)_2(SO_4)$ crystal was measured using a BX53MTRF-S polarizing microscope equipped with a Berek compensator. A transparent and clean flake of $Nb_2O_2(TeO_3)_2(SO_4)$ was selected for the measurement. The birefringence value (Δn) was calculated using the formula $\Delta R = \Delta n \times d$, where ΔR is the optical path difference and d is the thickness of the selected crystal.[52]

Theoretical calculations

First-principles calculations based on density functional theory (DFT) were performed using the Vienna *Ab initio* Simulation Package (VASP).[53,54] The DFT method has proven to be one of the most accurate methods for the computation of the electronic structure of solids.[55–61] The projector augmented wave (PAW)[62] pseudopotential method and the generalized gradient approximation (GGA)[63] of the Perdew–Burke–Ernzerhof (PBE) exchange–correlation energy functional were used. The cutoff energy was set as 500 eV. For geometry optimization, the first Brillouin zone was sampled using a Γ-centered k mesh of 5 × 5 × 5. The convergence threshold was set to be 1×10^5 eV in energy and 0.02 eV $Å^{-1}$ in force.

Results and discussion

Single-crystal X-ray diffraction analysis reveals that $Nb_2O_2(TeO_3)_2(SO_4)$ crystallizes in the non-centrosymmetric and polar space group *Cc* (no. 9), which corresponds to crystal class *m* (Schönflies symbol *Cs*). The lattice parameters are a = 20.0326(7) Å, b = 6.5977(3) Å, c = 7.6438(2) Å, β = 107.220(2) °, Z = 4 and V = 964.99(6) $Å^3$ (Table S1). The asymmetric unit contains two unique Nb atoms, two Te atoms, one S atom, and twelve unique O atoms. Each Te atom is bonded to three O atoms, forming a [TeO_3] pyramid containing SCALP electrons, with the Te–O bond lengths ranging from 1.814 to 1.954 Å (Table S3). The S atom is coordinated by four O atoms, generating a typical [SO_4] unit with S–O bond lengths ranging from 1.409 to 1.530 Å. Six O atoms coordinate the Nb atom to form a typical [NbO_6] octahedron, with Nb–O bond lengths in the range of 1.773–2.171 Å. In the crystal structure, the [NbO_6] octahedra share O atoms to form one-dimensional (1D) chains (Fig. S1). These chains are interconnected by [TeO_3] pyramids, giving rise to [$(NbO_1O_{5/2})_2(TeO_{3/2})_2$] layers parallel to the *bc* plane (Fig. 1a). These layers are further interconnected along the *a*-axis by [SO_4] tetrahedra to form a 3D framework of $Nb_2O_2(TeO_3)_2(SO_4)$ (Fig. 1b). It is noteworthy that one Nb atom in $Nb_2O_2(TeO_3)_2(SO_4)$ exhibits crystallographic disorder, occupying two distinct positions with site occupancy factors of 78% and 22%, corresponding to Nb2 and Nb2A, respectively. As shown in Fig. S2, influenced by the SOJT effect, all [NbO_6] octahedra exhibit clear separation into three long and three short Nb–O bonds, forming an asymmetric coordination environment, with bond length ranges of 2.014–2.127 Å and

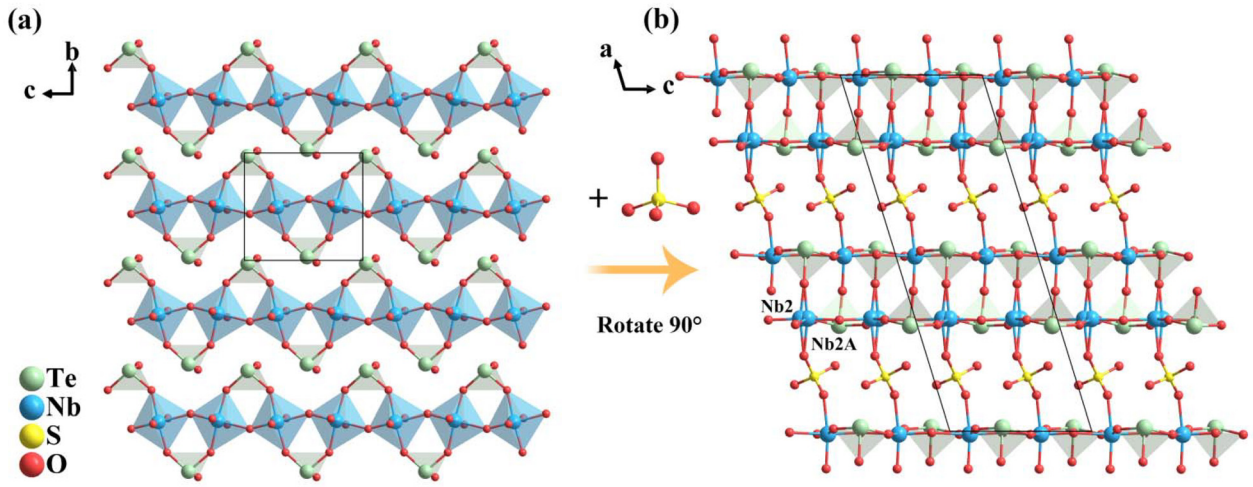

Fig. 1 Crystal structure of $Nb_2O_2(TeO_3)_2(SO_4)$ viewed along the (a) [100] and (b) [010] directions.

Published on 06 March 2026. Downloaded on 6/21/2026 11:58:36 AM.

1.816–1.946 Å for Nb1, 2.029–2.172 Å and 1.773–1.966 Å for Nb2, and 2.028–2.172 Å and 1.773–1.954 Å for Nb2A. Notably, the three long Nb–O bonds are preferentially oriented toward one side of the octahedron, while the three short bonds are clustered on the opposite side, resulting in an off-center displacement of the Nb atom. According to the classification proposed by Halasyamani,[64] the out-of-center distortion of the [NbO_6] octahedron in this structure can be classified as C_3[111]-type distortion. The calculated magnitudes of the octahedral out-of-center distortion (Δd) are 0.63 for the [Nb1O_6] octahedron, 0.60 for the [Nb2O_6] octahedron (78%), and 0.62 for the [Nb2AO_6] octahedron (22%), which is a moderate distortion. The calculated bond valence sums (BVSs) for Nb^{5+}, Te^{4+}, S^{6+}, and O^{2-} in $Nb_2O_2(TeO_3)_2(SO_4)$ are 5.18–5.32, 3.73–3.94, 6.10, and 1.65–2.22, respectively, which are consistent with their oxidation states (Table S2).[65,66]

PXRD analysis of $Nb_2O_2(TeO_3)_2(SO_4)$ was carried out to evaluate its phase purity. The experimental PXRD pattern matches well with the simulated pattern generated from the single-crystal X-ray diffraction data, confirming the phase purity of the sample and validating the accuracy of the refined crystal structure (Fig. S3). To assess the chemical stability, the samples were respectively immersed in water and concentrated sulfuric acid for 15 days and exposed to air for 6 months. No noticeable change in mass, appearance or morphology was observed, and the PXRD patterns remained consistent with those before treatment, confirming its excellent chemical stability in both water and concentrated sulfuric acid, as well as outstanding long-term environmental stability (Fig. S4).

To further investigate the thermal stability of $Nb_2O_2(TeO_3)_2(SO_4)$, TGA and DSC analyses were performed. The TGA curve indicates that the $Nb_2O_2(TeO_3)_2(SO_4)$ crystal exhibits almost no weight loss below 600 °C, and no obvious endothermic or exothermic peaks are observed in the DSC curve before 600 °C, suggesting that no decomposition occurs in this temperature range (Fig. S5). The thermal decomposition of $Nb_2O_2(TeO_3)_2(SO_4)$ proceeds in two stages. The first stage starts at approximately 600 °C and ends at 750 °C, with an observed weight loss of 12.54%, which agrees well with the theoretical value of 12.03% corresponding to the release of SO_3. The second stage occurs between 750 °C and 1200 °C and can be attributed to the decomposition of TeO_2. However, the tellurite species are not completely removed even at 1200 °C. According to previous reports, the thermal stability of this compound is second only to that of $Y_2(Te_4O_{10})(SO_4)$ among the known tellurium–sulfate systems (Table S5).[39] These results collectively demonstrate that $Nb_2O_2(TeO_3)_2(SO_4)$ possesses excellent thermochemical stability, providing a reliable structural basis for subsequent optical property measurements.

The IR spectrum of $Nb_2O_2(TeO_3)_2(SO_4)$ (4000–400 cm^{-1}, Fig. S6) provides stronger evidence for its structural model. No obvious characteristic absorption bands were observed between 4000 and 1350 cm^{-1}. The strong absorption bands in the range of 1200–950 cm^{-1} can be attributed to the stretching vibrations of S–O bonds, confirming the presence of [SO_4] tetrahedra. The characteristic peaks observed at 850–600 cm^{-1} and 400–510 cm^{-1} are attributed to the stretching vibrations of Te–O bonds, whereas the absorption band at 584 cm^{-1} originates from the characteristic stretching of Nb–O bonds. The positions of these characteristic bands are consistent with those reported for related compounds, further supporting the structural analysis results.[29,30,38,67]

Fig. 2 presents the UV-Vis-NIR diffuse reflectance spectra of $Nb_2O_2(TeO_3)_2(SO_4)$. The result shows an optical band gap of 3.2 eV, corresponding to an absorption edge at approximately 305 nm, indicating that $Nb_2O_2(TeO_3)_2(SO_4)$ is a potential UV optical material. The band structure diagram from DFT calculations indicates that $Nb_2O_2(TeO_3)_2(SO_4)$ is a direct band-gap semiconductor with a band gap of 2.8 eV (Fig. S7), 0.4 eV lower than the experimental one owing to the well-known discontinuity of the exchange–correlation potential within DFT–GGA calculations.[68]

The second-order NLO property of $Nb_2O_2(TeO_3)_2(SO_4)$ was evaluated by measuring the SHG response of the (100) crystal face under 1064 nm laser irradiation at varying power using an integrated frequency-doubling measurement system. The results demonstrate a marked increase in SHG intensity with incident laser power (Fig. 3a and Fig. S8). Furthermore, the logarithmic plot in Fig. 3b reveals that the SHG intensity exhibits a good linear relationship with the incident laser power, with a fitted slope of 1.96, consistent with the characteristics of a second-order NLO process.

To investigate the phase-matchable behaviour, the SHG intensities of $Nb_2O_2(TeO_3)_2(SO_4)$ samples with different particle sizes were measured and compared with those of KDP. As shown in Fig. 3c, the SHG signals of $Nb_2O_2(TeO_3)_2(SO_4)$ gradually increase with the particle size, indicating a phase-matchable behaviour. Quantitative analysis reveals that in the 150–214 μm size range, the SHG intensity of $Nb_2O_2(TeO_3)_2(SO_4)$ reaches approximately 0.82 times that of KDP, demonstrating a moderate frequency-doubling efficiency

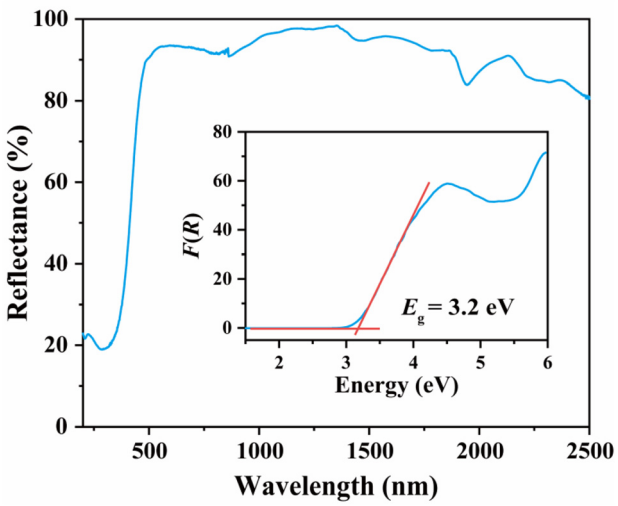

Fig. 2 UV-Vis-NIR diffuse reflectance spectra of $Nb_2O_2(TeO_3)_2(SO_4)$. The inset shows the band gap at ambient pressure.

This journal is © The Royal Society of Chemistry 2026

Published on 06 March 2026. Downloaded on 6/21/2026 11:58:36 AM.

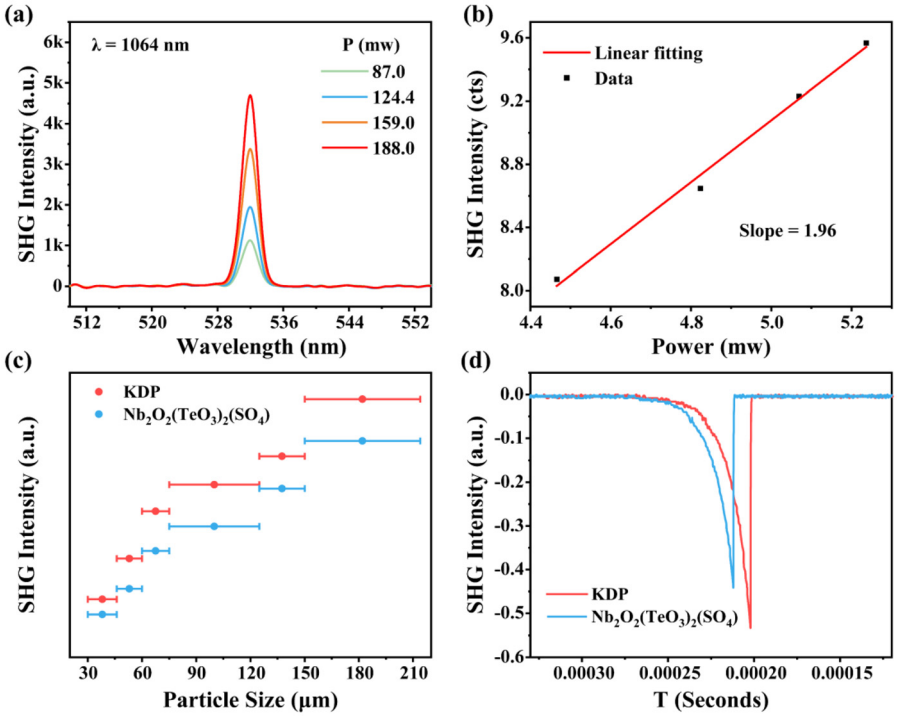

Fig. 3 (a) SHG intensity of $Nb_2O_2(TeO_3)_2(SO_4)$ under 1064 nm laser irradiation. (b) SHG intensity as a function of pump power on a logarithmic scale. (c) SHG intensity *versus* particle size for $Nb_2O_2(TeO_3)_2(SO_4)$ and KDP under 1064 nm laser irradiation. (d) Oscilloscope traces of the SHG signals of $Nb_2O_2(TeO_3)_2(SO_4)$ and KDP in the same particle size range of 150–212 μm.

and confirming its good NLO activity (Fig. 3d). To gain deeper insight into the structural origin of its NCS nature, which is a prerequisite for SHG activity, the dipole moments of the individual structural units were calculated (Table S6). The analysis reveals that the polarizations of the $[NbO_6]$, $[TeO_3]$, and $[SO_4]$ units cancel each other along the *y*-direction but constructively superimpose along the *x*- and *z*-directions. This NCS alignment of local dipoles results in a net macroscopic polarization, consistent with the observed SHG response. This polarization primarily stems from the synergistic contributions of the distorted $[NbO_6]$ octahedra, the lone-pair-active $[TeO_3]$ pyramids, and the $[SO_4]$ tetrahedra.

A sufficiently large birefringence (typically >0.02) is essential to ensure phase-matchable capability for potential NLO crystals.[31] The birefringence of $Nb_2O_2(TeO_3)_2(SO_4)$ was measured using a BX53MTRF-S polarized optical microscope equipped with a Berek compensator. A clean and transparent single crystal was selected for measurement, and the measured crystal plane is the (100) plane. The original interference color of the $Nb_2O_2(TeO_3)_2(SO_4)$ single crystal observed under cross-polarized light is fourth-order green, corresponding to an optical path difference of 1831.31 nm for a crystal thickness of 9.288 μm (Fig. 4a–c). Based on the optical path difference formula, the birefringence of the (100) plane was calculated to be approximately 0.197 at 546 nm. DFT calculations reveal that the refractive indices along the three optical principal axes follow the relationship $n_z > n_y \approx n_x$ (Fig. 4d). The computed birefringence value is 0.195 at 546 nm, in good agreement with the experimental observation. As shown in Table S7, in sulfate NLO crystals, although the birefringence of $Nb_2O_2(TeO_3)_2(SO_4)$ (0.197@546 nm) is surpassed by those of a few Ce-based compounds, this value significantly exceeds those of most known sulfate NLO materials, which is almost twice that of $Hg_2O_2SO_4$ (0.100@546 nm) and substantially larger than those of other prominent systems like $KBiCl_2SO_4$ (0.098@1064 nm) and $RbSbSO_4Cl_2$ (0.110@1064 nm).[69,70] This remarkable birefringence not only ensures phase-matchable capability but also demonstrates the effectiveness of combining $[NbO_6]$ and $[TeO_3]$ units for enhancing optical anisotropy in sulfate systems.

First-principles calculations were conducted to obtain deeper insight into the relationship between the internal structure and the optical properties of $Nb_2O_2(TeO_3)_2(SO_4)$. The total and partial density of states (TDOS/PDOS) of $Nb_2O_2(TeO_3)_2(SO_4)$ are presented in Fig. 5a. The results reveal significant overlap between the electronic states of Nb and O from the valence band (VB) to the conduction band (CB), alongside moderate Te–O overlap. This indicates that the Nb–O bonds possess strong covalent character, whereas the Te–O bonds exhibit partial covalency. The top of the valence band (−6 to 0 eV) is predominantly constituted by O-2p and Te-5p orbitals. In comparison, the bottom of the conduction band (2 to 7 eV) is dominated by Nb-4d states with a minor Te-5p contribution, suggesting that Nb and O primarily determine the band gap. Since the optical properties of the compound are mainly governed by orbitals near the Fermi level,

Published on 06 March 2026. Downloaded on 6/21/2026 11:58:36 AM.

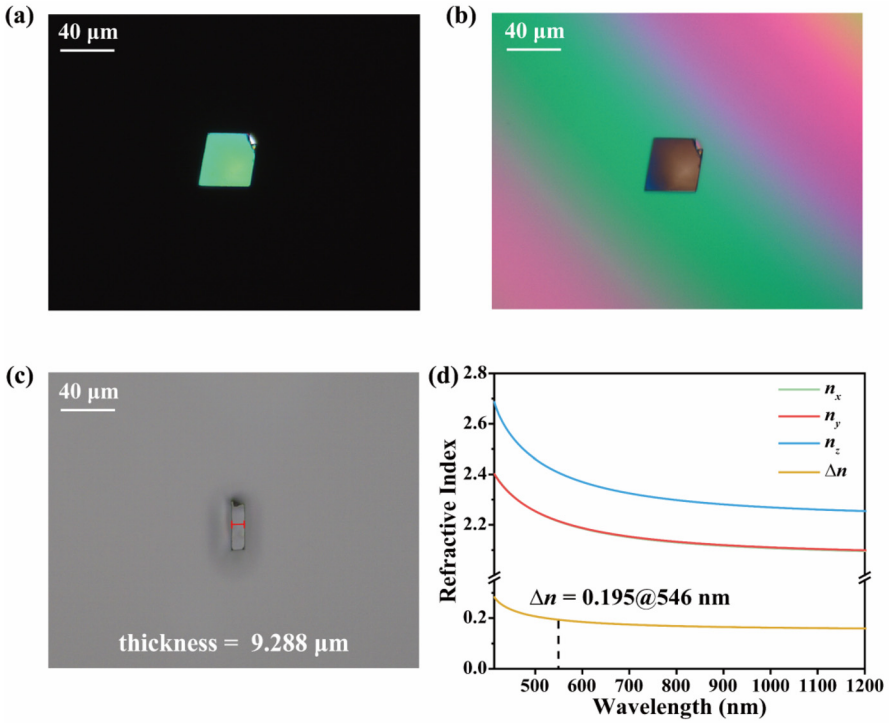

Fig. 4 (a) The original interference color of the $Nb_2O_2(TeO_3)_2(SO_4)$ single crystal under cross-polarized light. (b) The extinction of the $Nb_2O_2(TeO_3)_2(SO_4)$ single crystal. (c) The thickness of the single-crystal sample. (d) Calculated refractive index dispersion curves of $Nb_2O_2(TeO_3)_2(SO_4)$.

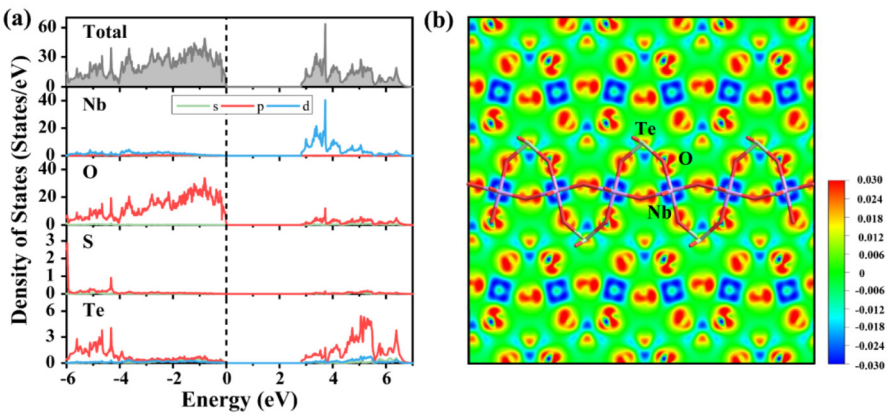

Fig. 5 (a) Total and partial density of states for $Nb_2O_2(TeO_3)_2(SO_4)$. (b) Electron density difference map of $Nb_2O_2(TeO_3)_2(SO_4)$.

the calculations indicate that its optical response arises primarily from the $[NbO_6]$ and $[TeO_3]$ units. Furthermore, the electron density difference (EDD) map confirms the strong covalent interactions between the Nb and O atoms, where the electron clouds will exhibit directional stretching and contraction along the external optical field, giving rise to a pronounced polarization effect (Fig. 5b). These features underline that the Nb–O bonds play a dominant role in the NLO activity. Additionally, it is clearly described that Te^{4+} has SCALP electrons. Therefore, the primary origin of this large birefringence is the highly anisotropic polarizability tensor produced by (i) directional Nb–O covalent bonds that induce strong electronic delocalization along specific crystallographic axes and (ii) the SCALP electrons on Te^{4+}, which increase local polarizability and reinforce optical anisotropy; together these effects generate a large difference in refractive index between orthogonal directions (Δn), accounting for the measured birefringence. Consequently, these analyses indicate that the $[NbO_6]$ and $[TeO_3]$ groups significantly enhance SHG response and birefringence in sulfate-based systems.

 This journal is © The Royal Society of Chemistry 2026

Published on 06 March 2026. Downloaded on 6/21/2026 11:58:36 AM.

Conclusions

In conclusion, we successfully synthesized a novel UV-NLO sulfate crystal $Nb_2O_2(TeO_3)_2(SO_4)$ guided by a double SOJT strategy. This compound overcomes the inherent limitations of sulfates by exhibiting an exceptional combination of a remarkable birefringence (0.197@546 nm), a moderate SHG response (0.82 × KDP), and a wide UV transparency window. Also, its practical applicability is further underscored by outstanding thermochemical stability. First-principles calculations reveal that the synergistic effect between the $[NbO_6]$ octahedra and the $[TeO_3]$ pyramids is the fundamental origin of the enhanced optical properties. This work not only presents a good-performance candidate for UV-NLO applications but also validates an effective strategy for the rational design of functional materials.

Author contributions

Prof. Liujiang Zhou provided research ideas, supervised the entire research, and revised the manuscript. Prof. Weizhao Cai offered help with data and experimental analysis and revised the manuscript. Jingsha Xu initially drafted and completed the entire experiment and measurement work. Dr Xiaofeng Zhang is responsible for theoretical calculations. Shanshan Chen, Weiyi Wang and Wenbo Qiu assisted in the experiments and measurements. All the authors participated in the discussion.

Conflicts of interest

The authors declare no competing financial interest.

Data availability

The data supporting this article have been included as part of the supplementary information (SI). Supplementary information: measurement results and details of $Nb_2O_2(TeO_3)_2(SO_4)$ (Fig. S1–S8), crystallographic data and structural data (Tables S1–S4), a comparative table of tellurate sulfates (Table S5), dipole moments (Table S6), and a comparative table of sulfates (Table S7). See DOI: https://doi.org/10.1039/d5dt03078a.

CCDC 2501214 ($Nb_2O_2(TeO_3)_2(SO_4)$) contains the supplementary crystallographic data for this paper.[71]

Acknowledgements

This work was supported by the National Natural Science Foundation of China (Grant No. 12374057 and 12274062) and the Natural Science Foundation of Sichuan Province (Grant No. 2026NSFSC0030).

References

1 N. Savage, *Nat. Photonics*, 2007, **1**, 83–85.
2 D. Cyranoski, *Nature*, 2009, **457**, 953–955.
3 M. Mutailipu, K. R. Poeppelmeier and S. Pan, *Chem. Rev.*, 2021, **121**, 1130–1202.
4 Y. Wu, T. Sasaki, S. Nakai, A. Yokotani, H. Tang and C. Chen, *Appl. Phys. Lett.*, 1993, **62**, 2614–2615.
5 P. S. Halasyamani and W. Zhang, *Inorg. Chem.*, 2017, **56**, 12077–12085.
6 C. Wu, T. Wu, X. Jiang, Z. Wang, H. Sha, L. Lin, Z. Lin, Z. Huang, X. Long, M. G. Humphrey and C. Zhang, *J. Am. Chem. Soc.*, 2021, **143**, 4138–4142.
7 T. T. Tran, H. Yu, J. M. Rondinelli, K. R. Poeppelmeier and P. S. Halasyamani, *Chem. Mater.*, 2016, **28**, 5238–5258.
8 G. Yi and G. Zou, *Chin. J. Struct. Chem.*, 2023, **42**, 100020.
9 X. Dong, L. Huang, H. Zeng, Z. Lin, K. M. Ok and G. Zou, *Angew. Chem., Int. Ed.*, 2022, **61**, e202116790.
10 Y. Pan, S. P. Guo, B. W. Liu, H. G. Xue and G. C. Guo, *Coord. Chem. Rev.*, 2018, **374**, 464–496.
11 X. Dong, L. Huang, C. Hu, H. Zeng, Z. Lin, X. Wang, K. M. Ok and G. Zou, *Angew. Chem., Int. Ed.*, 2019, **58**, 6528–6534.
12 F. Yang, L. Huang, X. Zhao, L. Huang, D. Gao, J. Bi, X. Wang and G. Zou, *J. Mater. Chem. C*, 2019, **7**, 8131–8138.
13 F. Yang, L. Wang, Y. Ge, L. Huang, D. Gao, J. Bi and G. Zou, *J. Alloys Compd.*, 2020, **834**, 155154.
14 F. He, Q. Wang, M. Liu, L. Huang, D. Gao, J. Bi and G. Zou, *Cryst. Growth Des.*, 2018, **18**, 4756–4765.
15 S. Zhao, Y. Yang, Y. Shen, B. Zhao, L. Li, C. Ji, Z. Wu, D. Yuan, Z. Lin, M. Hong and J. Luo, *Angew. Chem., Int. Ed.*, 2017, **56**, 540–544.
16 S. Zhao, L. Kang, Y. Shen, X. Wang, M. A. Asghar, Z. Lin, Y. Xu, S. Zeng, M. Hong and J. Luo, *J. Am. Chem. Soc.*, 2016, **138**, 2961–2964.
17 A. H. Reshak, *J. Alloys Compd.*, 2017, **722**, 438–444.
18 Y. Zhang, Y. Long, X. Dong, L. Wang, L. Huang, H. Zeng, Z. Lin, X. Wang and G. Zou, *Chem. Commun.*, 2019, **55**, 4538–4541.
19 S. Zhao, P. Gong, S. Luo, S. Liu, L. Li, M. A. Asghar, T. Khan, M. Hong, Z. Lin and J. Luo, *J. Am. Chem. Soc.*, 2015, **137**, 2207–2210.
20 A. H. Reshak and S. Auluck, *Phys. Chem. Chem. Phys.*, 2017, **19**, 18416–18425.
21 W. Huang, X. Zhang, Y. Li, Y. Zhou, X. Chen, X. Li, F. Wu, M. Hong, J. Luo and S. Zhao, *Angew. Chem., Int. Ed.*, 2022, **61**, e202202746.
22 A. H. Reshak and S. Auluck, *RSC Adv.*, 2017, **7**, 14752–14760.
23 J. Xue, S. Wang, X. Peng, Z. Lin, X. Dong, L. Cao, L. Huang and G. Zou, *Inorg. Chem.*, 2025, **64**, 2133–2139.
24 R. Priya, S. Krishnan, C. J. Raj and S. J. Das, *Cryst. Res. Technol.*, 2009, **44**, 1272–1276.
25 Y. Li, C. Yin, X. Yang, X. Kuang, J. Chen, L. He, Q. Ding, S. Zhao, M. Hong and J. Luo, *CCS Chem.*, 2020, **3**, 2298–2306.

Published on 06 March 2026. Downloaded on 6/21/2026 11:58:36 AM.

26 Y. Li, F. Liang, S. Zhao, L. Li, Z. Wu, Q. Ding, S. Liu, Z. Lin, M. Hong and J. Luo, *J. Am. Chem. Soc.*, 2019, **141**, 3833–3837.
27 M. Ya. Rudysh, V. Yo. Stadnyk, P. A. Shchepanskyi, R. S. Brezvin, J. Jedryka and I. V. Kityk, *Physica B: Condens. Matter*, 2020, **580**, 411919.
28 Z. H. Yue, Z. T. Lu, H. G. Xue and S. P. Guo, *Cryst. Growth Des.*, 2019, **19**, 3843–3850.
29 Y. Song, X. Hao, C. Lin, D. Lin, M. Luo and N. Ye, *Inorg. Chem.*, 2021, **60**, 11412–11418.
30 H. Tang, Y. Zhang, C. Zhuo, R. Fu, H. Lin, Z. Ma and X. Wu, *Angew. Chem., Int. Ed.*, 2019, **58**, 3824–3828.
31 Z. Li, Z. Liang, J. Wan, L. Liu, C. Wu, P. Wang, X. Jiang, Z. Lin and H. Liu, *Chem. Sci.*, 2025, **16**, 3329–3335.
32 L. Lin, X. Jiang, C. Wu, L. Li, Z. Lin, Z. Huang, M. G. Humphrey and C. Zhang, *ACS Appl. Mater. Interfaces*, 2020, **12**, 49812–49821.
33 J. D. Bierlein and H. Vanherzeele, *J. Opt. Soc. Am. B*, 1989, **6**, 622–633.
34 G. D. Boyd, R. C. Miller, K. Nassau, W. L. Bond and A. Savage, *Appl. Phys. Lett.*, 1964, **5**, 234–236.
35 K. M. Ok, P. S. Halasyamani, D. Casanova, M. Llunell, P. Alemany and S. Alvarez, *Chem. Mater.*, 2006, **18**, 3176–3183.
36 M. Kunz and I. D. Brown, *J. Solid State Chem.*, 1995, **115**, 395–406.
37 P. F. Li, C. L. Hu, Y. P. Gong, F. Kong and J. G. Mao, *Chem. Commun.*, 2021, **57**, 7039–7042.
38 Y. P. Gong, Y. X. Ma, S. M. Ying, J. G. Mao and F. Kong, *Inorg. Chem.*, 2019, **58**, 11155–11163.
39 P. F. Li, C. L. Hu, F. Kong, S. M. Ying and J. G. Mao, *Inorg. Chem. Front.*, 2021, **8**, 164–172.
40 P. F. Li, C. L. Hu, Y. F. Li, J. G. Mao and F. Kong, *J. Am. Chem. Soc.*, 2024, **146**, 7868–7874.
41 D. Wei, J. Bai, Y. Huang and H. J. Seo, *Appl. Surf. Sci.*, 2020, **533**, 147502.
42 A. W. Hewat, *J. Phys. C: Solid State Phys.*, 1973, **6**, 2559.
43 G. Foulon, A. Brenier, M. Ferriol, M. T. Cohen-Adad and G. Boulon, *J. Lumin.*, 1997, **72–74**, 794–796.
44 Z. Cheng, X. Wang, K. Ozawa and H. Kimura, *J. Cryst. Growth*, 2007, **307**, 353–357.
45 T. Zhang, J. Jiao, W. Zhao, F. Wang, F. Liang, N. Ye, Z. Hu, Y. Wu and C. Li, *Inorg. Chem.*, 2023, **62**, 17522–17529.
46 H. S. Ra, K. M. Ok and P. S. Halasyamani, *J. Am. Chem. Soc.*, 2003, **125**, 7764–7765.
47 Bruker, *APEX5 (Version 2023.9-2). Program for Data Collection on Area Detectors*, Bruker AXS Inc., Madison, Wisconsin, USA, 2023.
48 G. M. Sheldrick, *Acta Crystallogr., Sect. A: Found. Crystallogr. Acta Crystallogr., Sect. A: Found. Crystallogr.*, 2008, **64**, 112–122.
49 S. Chen, Z. Bai, X. Song, T. Ouyang, Y. Li, Q. Ding, H. Wang, W. Chen, J. Luo and S. Zhao, *Small*, 2025, **21**, 2408191.
50 P. Kubelka and F. Munk, *Z. Tech. Phys.*, 1931, **12**, 593–601.
51 S. K. Kurtz and T. T. Perry, *J. Appl. Phys.*, 1968, **39**, 3798–3813.
52 L. Cao, G. Peng, W. Liao, T. Yan, X. Long and N. Ye, *CrystEngComm*, 2020, **22**, 1956–1961.
53 G. Kresse and J. Furthmüller, *Phys. Rev. B: Condens. Matter Mater. Phys.*, 1996, **54**, 11169–11186.
54 G. Kresse and J. Furthmüller, *Comput. Mater. Sci.*, 1996, **6**, 15–50.
55 S. Tabassam, A. H. Reshak, G. Murtaza, S. Muhammad, A. Laref, M. Yousaf, A. M. Al Bakri and J. Bila, *J. Mol. Graphics Modell.*, 2021, **104**, 107841.
56 D. M. Hoat, S. Amirian, H. Alborznia, A. Laref, A. H. Reshak and M. Naseri, *Indian J. Phys.*, 2021, **95**, 2365–2373.
57 M. Husain, N. Rahman, A. H. Reshak, Z. Ahmad, A. Habib, S. Ali, A. Laref, A. M. M. Al Bakri and J. Bila, *Eur. Phys. J. Plus*, 2021, **136**, 624.
58 R. Singla, S. Kumar, T. A. Hackett, A. H. Reshak and M. K. Kashyap, *J. Alloys Compd.*, 2021, **859**, 157776.
59 A. Hassan, M. Ismail, A. H. Reshak, Z. Zada, A. A. Khan, M. Fazal Ur Rehman, M. Arif, K. Siraj, S. Zada, G. Murtaza and M. M. Ramli, *J. Mol. Struct.*, 2023, **1274**, 134484.
60 H. Yu, H. Huang, A. H. Reshak, S. Auluck, L. Liu, T. Ma and Y. Zhang, *Appl. Catal., B*, 2021, **284**, 119709.
61 R. Ullah, A. H. Reshak, M. A. Ali, A. Khan, G. Murtaza, M. Al Anazy, H. Althib and T. H. Flemban, *Int. J. Energy Res.*, 2021, **45**, 8711–8723.
62 P. E. Blöchl, *Phys. Rev. B: Condens. Matter Mater. Phys.*, 1994, **50**, 17953–17979.
63 J. P. Perdew, K. Burke and M. Ernzerhof, *Phys. Rev. Lett.*, 1996, **77**, 3865–3868.
64 P. S. Halasyamani, *Chem. Mater.*, 2004, **16**, 3586–3592.
65 I. D. Brown and D. Altermatt, *Acta Crystallogr., Sect. B: Struct. Sci.*, 1985, **41**, 244–247.
66 N. E. Brese and M. O'Keeffe, *Acta Crystallogr., Sect. B: Struct. Sci.*, 1991, **47**, 192–197.
67 Q. H. Gu, C. L. Hu, J. H. Zhang and J. G. Mao, *Dalton Trans.*, 2011, **40**, 2562.
68 A. J. Cohen, P. Mori-Sánchez and W. Yang, *Phys. Rev. B: Condens. Matter Mater. Phys.*, 2008, **77**, 115123.
69 T. Wu, X. Jiang, Y. Zhang, Z. Wang, H. Sha, C. Wu, Z. Lin, Z. Huang, X. Long, M. G. Humphrey and C. Zhang, *Chem. Mater.*, 2021, **33**, 9317–9325.
70 F. He, Y. Deng, X. Zhao, L. Huang, D. Gao, J. Bi, X. Wang and G. Zou, *J. Mater. Chem. C*, 2019, **7**, 5748–5754.
71 CCDC 2501214, Experimental Crystal Structure Determination, 2026, DOI: 10.25505/fiz.icsd.cc2pyqbq.

This journal is © The Royal Society of Chemistry 2026